Elucidation of the Ro-Vibrational Band Structures in the Silicon Tetrafluoride Spectra from Accurate Ab Initio Calculations

Oleg Egorov, Michael M. Rey

Elucidation of the ro-vibrational band structures in the silicon tetrafluoride spectra from accurate *ab initio* calculations

Oleg Egorov [1] and Michaël Rey [2,*]

[1] Laboratory of Theoretical Spectroscopy, V.E. Zuev Institute of Atmospheric Optics SB RAS 1, Akademician Zuev Sq., Tomsk, 634055 Russia
[2] Groupe de Spectrométrie Moléculaire et Atmosphérique UMR CNRS 7331, UFR Sciences BP 1039, 51687 Reims Cedex 2, France
* Correspondence: michael.rey@univ-reims.fr

Abstract

We report the construction of comprehensive line lists for the three stable isotopologues of silicon tetrafluoride ($^{28}SiF_4$, $^{29}SiF_4$, and $^{30}SiF_4$) using a new effective Hamiltonian and dipole moment model built from accurate *ab initio* potential energy and dipole moment surfaces developed in this work. The vibrational energy levels were grouped into a series of polyads up to P_{max}=19, while the ro-vibrational energy levels were computed up to J_{max}=99. Each line list covers the spectral range [0–2500] cm^{-1} and contains almost 500 million transitions at T=296 K, generated from 685 vibrational states and sub-states. Most of the cold and hot band transitions computed in this work were not available in the literature so far. The absorption cross sections computed from the produced line lists were successfully validated by direct comparison with the experimental data measured by Pacific Northwest National Laboratory at room temperature. Most of the ro-vibrational band structures observed in the experimental spectra can be now elucidated using the line lists proposed in this work.

Keywords: SiF_4, silicon tetrafluoride, *ab initio* calculations, global line list, effective model, infrared spectra

1. Introduction

Chemically, silicon tetrafluoride (SiF_4) is a gas with high thermal stability compared to other silicon tetrahalides. The origin of the strong chemical bonds in SiF_4 can be explained by the orbital energies: the 2p valence orbitals of each F atom closely match the energy of the 3s and 3p valence orbitals of the silicon atom. As a result, the Si-F bond length in SiF_4 is unusually short compared to that in $SiHF_3$, SiH_2F_2, and SiH_3F (see, *e.g.*, Wang *et al*. [1] for further details).

Environmentally, SiF_4 is pollutant gas widely produced in microelectronics as a by-product in the etching of Si-based materials (Hada *et al*. [2]). Since fluorine is monoisotopic, $^{28}SiF_4$ holds potential for producing isotopically pure (^{28}Si) semiconductors (Ernst *et al*. [3]).

The abundance of SiF_4 is related to that of hydrogen fluoride (HF). The highly toxic HF can be produced by hydrolysis of SiF_4, a complex multistage chemical process (Ignatov *et al*. [4], Sennikov *et al*. [5]). HF synthesis is also possible *via* a mixture of SiF_4 and H_2 under

low-pressure microwave plasma conditions (Liu *et al*. [6]). SiF_4 has been detected in volcanic plumes of different volcanoes, in particular, Mt. Etna, Vulcano (by Francis *et al*. [7]), Popocatépetl (by Love *et al*. [8], Stremme *et al*. [9], Taquet *et al*. [10, 11]), and Satsuma-Iwojima (by Mori *et al*. [12]). It is assumed that SiF_4 arises from the interaction between magmatic HF and siliceous rocks (SiO_2).

From a spectroscopic point of view, SiF_4 is a heavy, rigid molecule with only small amplitude motions and whose vibrations exhibit a harmonic character up to high vibrational quantum numbers. This enables fast convergence of the Taylor series expansions, making the use of empirically-based effective models relevant (see, *e.g*., the empirical studies on overtone and combination bands by Patterson and Pine [13], McDowell *et al*. [14], and the theoretical study by Wang *et al*. [15] on the high-order canonical Van Vleck perturbation theory).

Due to its tetrahedral (T_d) symmetry, SiF_4 has no permanent dipole moment, making its pure rotational transitions extremely weak and challenging to measure (see, *e.g*., the recent paper by Simon *et al*. [16] on CF_4). Early spectroscopic studies first focused on the infrared active fundamental bands $\nu_3(F_2)$ and $\nu_4(F_2)$ of the main $^{28}SiF_4$ isotopologue. High-resolution Doppler-limited analyses of $\nu_3(F_2)$ and $\nu_4(F_2)$ were conducted by Patterson *et al*. [17] and McDowell *et al*. [14], respectively, using tunable diode lasers. Takami and Kuze [18] measured rotational transitions within the excited (0010) vibrational state using an infrared- microwave double resonance technique, which allowed the determination of rotational and centrifugal distortion parameters for the ground vibrational state. Later, Jörissen *et al*. [19] significantly extended the set of empirically-determined effective Hamiltonian parameters by combining new infrared data for the $\nu_3(F_2)$ band with rotational transitions, including those of the ground vibrational state (see also Ref. [20]).

Unlike early works, the recent high-resolution studies by Boudon *et al*. [21, 22] and Merkulova *et al*. [23] were focused on all three isotopologues simultaneously: $^{28}SiF_4$, $^{29}SiF_4$, and $^{30}SiF_4$. Given the relatively high abundances of $^{29}SiF_4$ and $^{30}SiF_4$ (4.7 % and 3.1 %, respectively), some of their absorption features are clearly distinguishable in the spectrum of natural SiF_4 (hereafter, "natural" means that all the three isotopologues are presented), particularly in the region of the strongest $\nu_3(F_2)$ band. Boudon *et al*. [21] used FTIR measurements based on the synchrotron radiation to assign the $\nu_3(F_2)$ and $\nu_4(F_2)$ bands of all three isotopologues. Moreover, the line positions of the $2\nu_4(F_2)$ band of $^{28}SiF_4$ were assigned for the first time. The line positions of the combination bands $\nu_2+\nu_3(F_1, F_2)$, $\nu_1+\nu_4(F_2)$, $\nu_2+\nu_4(F_1, F_2)$ were also assigned and fitted for $^{28}SiF_4$, while $\nu_1+\nu_3(F_2)$ was analyzed for all three isotopologues in Ref. [23].

Despite recent progress, the available room temperature line lists for such heavy molecules are far to be complete. Indeed, at T=296 K SiF_4 exhibits a very dense and congested spectrum due to a tremendous number of hot transitions. As a result, most of the recent studies have been focused essentially on lower temperatures (*e.g*., at T=160 K in Ref. [21]). As demonstrated in this work, nearly half a billion transitions were needed to converge the sum of intensities at T=296 K in the spectral region [0–2500] cm^{-1}, using a new effective model which is able to predict more than 2000 bands and sub-bands. Needless to say that such a vast amount of data is difficult to extract from experimental spectra. Therefore, this work extends the current knowledge on the SiF_4 spectra and supplements the results presented in the recently made empirical database TFSiCaSDa (Richard et al. [24]).

In this study, we present global line lists for $^{28}SiF_4$, $^{29}SiF_4$, and $^{30}SiF_4$ computed from extensive quantum-chemical and advanced nuclear-motion calculations. First *ab initio* potential energy and dipole moment surfaces (hereafter, PES and DMS) have been constructed and presented in Sections 2 and 3. Then, the Watson-Eckart nuclear-motion Hamiltonian was employed to compute variational eigenpairs up to J=15 before applying a numerical block-diagonalization procedure to build a full effective polyad model (Section

4). The ro-vibrational energy levels enabled computation of the partition function required for the Boltzmann distribution (Section 5). We also investigated how optimal cut-off values for the rotational angular momentum (J) and line intensities can be chosen (Section 6). Finally, simulated absorption cross-sections of natural SiF_4 were validated against experimental data from the Pacific Northwest National Laboratory (hereafter, PNNL) [25] (Section 7).

2. Analytical model of the PES and DMS

The analytical model of the PES (V) and DMS (μ) was expressed as a Taylor series expansion in terms of irreducible tensor operators (ITOs) Ω_j^p

$$V \text{ or } \mu = \sum_{p=0}^{p_{\max}} \sum_j C_j \cdot \Omega_j^p , \quad (1)$$

where C_j are expansion coefficients to be fitted, while each ITO of degree p in the symmetry coordinates is expressed as

$$\Omega_j^p = \sum_{i=1}^{n} T_i \cdot \left[S_1^{A_1}\right]^{p_i^1} \cdot \left[S_2^{E}\right]^{p_i^2} \cdot \left[S_3^{F_2}\right]^{p_i^3} \cdot \left[S_4^{F_2}\right]^{p_i^4} . \quad (2)$$

Here, the expansion coefficients T_i are computed from the T_d Clebsch-Gordan coupling coefficients. Each term in Equation (1) is of order p and transforms as the totally irreducible representation A_1 of the T_d point group for the PES and as F_2 for the DMS. Since SiF_4 is a spherical top molecule, only one component of the DMS is necessary. In this work, we considered the x component ($\mu \equiv \mu_x$). The definition of the one- ($S_1^{A_1}$), two- (S_2^{E}), and three- ($S_3^{F_2}$ and $S_4^{F_2}$) dimensional symmetry coordinates as a function of the internal ones is given in Figure 1.

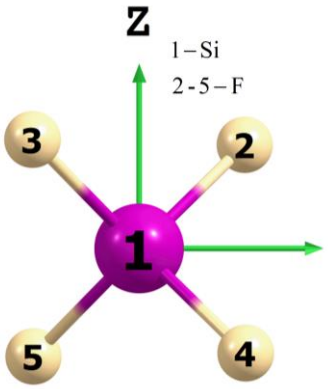

$$r_i = r_{1i+1}; \qquad \Delta r_i = r_i - r_e;$$
$$\alpha_1 = \angle 415;\ \alpha_2 = \angle 315;\ \alpha_3 = \angle 314; \qquad \Delta\alpha_i = \alpha_i - \alpha_e;\quad \Delta\beta_i = \beta_i - \beta_e;$$
$$\beta_1 = \angle 213;\ \beta_2 = \angle 214;\ \beta_3 = \angle 215. \qquad \alpha_e = \beta_e = 2\arctan\left(\sqrt{2}\right).$$
$$S_1^{A_1} = \left(\Delta r_1 + \Delta r_2 + \Delta r_3 + \Delta r_4\right)/2; \quad S_3^{F_2} = \begin{cases} \left(\Delta r_1 - \Delta r_2 + \Delta r_3 - \Delta r_4\right)/\sqrt{2} \\ \left(\Delta r_1 - \Delta r_2 - \Delta r_3 + \Delta r_4\right)/\sqrt{2} \\ \left(\Delta r_1 + \Delta r_2 - \Delta r_3 - \Delta r_4\right)/\sqrt{2} \end{cases};$$
$$S_2^{E} = \begin{cases} \left(2\Delta\alpha_1 - \Delta\alpha_2 - \Delta\alpha_3 + 2\Delta\beta_1 - \Delta\beta_2 - \Delta\beta_3\right)/\sqrt{12} \\ \left(\Delta\alpha_2 - \Delta\alpha_3 + \Delta\beta_2 - \Delta\beta_3\right)/2.0 \end{cases}; S_4^{F_2} = \begin{cases} \left(\Delta\alpha_2 - \Delta\beta_2\right)/\sqrt{2} \\ \left(\Delta\alpha_3 - \Delta\beta_3\right)/\sqrt{2} \\ \left(\Delta\alpha_1 - \Delta\beta_1\right)/\sqrt{2} \end{cases}.$$

Figure 1. Definition of the internal and symmetry coordinates for SiF_4.

The use of symmetry coordinates combined with ITOs allow to reduce significantly the number of unknown expansion coefficients C_j, as each ITO in Equation (2) is a polynomial function in S. Using ITOs allows to generate easily a compact set of linearly-independent parameters to be fitted to the *ab initio* grid, even for non-Abelian point groups as T_d. Previously, the ITO formalism was successfully employed to construct the PESs of different polyatomic molecules, including those of T_d symmetry as CF_4 [26].

The grid of reference nuclear configurations was made by varying the symmetry coordinates according to the nonzero symmetry components of ITOs. As illustrated in Figure 1, the deviation of the symmetry coordinates from zero results in corresponding deviations of the internal coordinates from their equilibrium values. However, to ensure an

unambiguous correspondence between the internal coordinates used in this work and those employed in *ab initio* packages as MOLPRO, all *ab initio* calculations were performed using the 3*N* Cartesian coordinates (here, *N*=5). The Cartesian coordinates were obtained by solving a system of 3*N* equations

$$\begin{cases} \mathbf{S} = \mathbf{I}, \\ \sum_{i=1}^{5} m_i \mathbf{d}_i = 0, \\ \sum_{i=1}^{5} m_i \left(\mathbf{a}_i^{ref} \times \mathbf{d}_i \right) = 0. \end{cases} \quad (3)$$

In Equation (3), $\mathbf{S}$ is the column vector consisting of the 9 symmetry coordinates (see Figure 1), while $\mathbf{I}$ represents their deviations from zero, which are unique for each point of our grid. The vectors $\mathbf{d}_i$ denote the Cartesian displacements of the *i*-th atom from the reference Cartesian position contained in the vector $\mathbf{a}_i^{ref}$. The last six equations in Equation (3) correspond to the first and second Eckart constraint conditions for rigid molecules (see, *e.g.*, Papoušek and Aliev [27]). The reference Cartesian vector is defined such that the atoms are positioned at the corners of the cube with side length of $2r_e / \sqrt{3}$. The relation between the symmetry and Cartesian coordinates in Equation (3) was established by using the standard formulas

$$\begin{cases} \mathbf{q}_i = \mathbf{a}_{i+1}^{ref} + \mathbf{d}_{i+1} - \mathbf{a}_1^{ref} - \mathbf{d}_1, \\ r_i = \sqrt{q_{ix}^2 + q_{iy}^2 + q_{iz}^2}, \quad i = 1..4; \\ \alpha_i(\beta_i) = \arccos\left[\left(q_{jx} q_{kx} + q_{jy} q_{ky} + q_{jz} q_{kz} \right) / \left(r_j r_k \right) \right], \quad i = 1..3, \\ j = 3, 2, 2(1,1,1); k = 4, 4, 3(2,3,4). \end{cases} \quad (4)$$

Finally, to fit the *ab initio* points it is more convenient to use Morse-cosine functions

$$\begin{aligned} y_{1..4} &= 1 - \exp\left[-1.5 \left(r_{1..4} - r_e \right) \right], \\ a_{1..3} &= \cos\left(\alpha_{1..3} \right) - \cos\left(\alpha_e \right), \quad b_{1..3} = \cos\left(\beta_{1..3} \right) - \cos\left(\beta_e \right) \end{aligned} \quad (5)$$

instead of the $\Delta r_{1..4}$, $\Delta\alpha_{1..3}$, and $\Delta\beta_{1..3}$ displacements involved in the symmetry coordinates (see Figure 1). The use of Equation (5) improves the asymptotic behavior beyond the reference nuclear configurations.

3. *Ab initio* calculations

3.1. PES

The *ab initio* electronic structure calculation for SiF_4 is computationally demanding because it requires computing the correlation energy for 50 electrons. To our knowledge, no full-dimensional *ab initio* PES for SiF_4 has been developed so far. On the other hand, SiF_4 is ideally suited to apply a single-reference approach, as the vertical excitation energies to the nearest triplet and single excited electronic states are extremely high compared to the IR spectral range – 98700 and 100250 cm^{-1}, respectively, as estimated in this work at the CAS(24, 16)/MRCISD(Q)/AVQZ level of the theory.

To achieve an accuracy of ~1 cm^{-1} when predicting the vibrational band origins from the *ab initio* PES, the orbital basis set size must approach the complete basis set (CBS) limit. Furthermore, corrections due to high-order electronic correlations, scalar relativistic effects and diagonal Born-Oppenheimer corrections (DBOC) must be also included. In this study, we have developed two *ab initio* PESs for SiF_4 (hereafter referred to as PES_I and

PES_II), based on the simplified explicitly correlated [RHF-CCSD(T)-F12x{x=a, b}] methods by Knizia *et al*. [28] and implemented in MOLPRO (by Werner *et al*. [29, 30]).

For PES_I, the RHF-CCSD(T)-F12a method was combined with the VTZ-F12 basis set. This type of approach is already known in the literature for van der Waals complexes and other many-electron systems. The calculations were performed on a grid (Grid_I) consisting of 8440 nuclear configurations generated using the 8th order ITOs. The resulting *ab initio* energies were thus fitted using 192 expansion coefficients (see Equation (1)) with a root mean square (RMS) deviation of 0.02 cm^{-1}.

Table 1. Fundamental band origins (in cm^{-1}) of $^{28}SiF_4$ variationally calculated (see Section 4) using the two "pure" *ab initio* PESs developed in this work

Band	Empirical (Boudon *et al*. [22])	*Ab initio* (This work) [1]		Final PES
		PES_I	PES_II	PES_II_refined
$\nu_2(E)$	264.219525(32)	261.462	263.582	264.2189
$\nu_4(F_2)$	388.433276(29)	384.898	387.785	388.4330
$\nu_1(A_1)$	800.66566(11)	795.882	799.989	800.6650
$\nu_3(F_2)$	1031.544438(65)	1025.575	1030.904	1031.5439
r_e(Si-F)	1.5516985(30)	1.558392	1.552765	1.551592

[1] PES_I corresponds to the CCSD(T)-F12a/VTZ-F12 level of the theory; PES_II is based on the CCSD(T)-F12b/CVQZ-F12 method (core-core, core-valence, and valence-valence correlations are included) in a combination with the correction from the high-order electronic correlations [CCSDT(Q)/VDZ]. The final PES was obtained from PES_II by the simultaneous empirical refining of its seconds derivatives (or harmonic frequencies) and equilibrium geometry (r_e in Ang.).

According to Table 1, PES_I is able to predict the fundamental band origins with an average absolute error of ~4 cm^{-1}. This turns out to be a good result given the relatively modest computational cost of the RHF-CCSD(T)-F12a/VTZ-F12 approach. Specifically, this approach is about 75 times faster per point than the "standard" RHF-CCSD(T) method combined with the aug-cc-pV5Z basis set, while it is only 7 times slower than the rough RHF-CCSD(T)/VTZ approach.

In order to compute the correlation energy from all electrons of SiF_4 (*i.e.*, core-core, core-valence, and valence-valence contributions), the RHF-CCSD(T)-F12b method was combined with the CVQZ-F12 basis set. Additionally, a smaller grid (Grid_II) consisting of 178 nuclear configurations was constructed using ITOs expanded up to the 4th order. Single-point calculations took up to 2 hours for the D_2 and C_2 symmetries and up to 8 hours without any symmetry.

Based on earlier benchmark calculations (*e.g.*, for the S_2O molecule with 40 electrons [31]), it is known that the explicitly correlated RHF-CCSD(T)-F12b/CVQZ-F12 approach provides results comparable with the aug-cc-pCV5Z basis set associated with the RHF-CCSD(T) method. However, when core electrons are included, corrections from high-order Slater determinants are required; otherwise the predicted band origins tend to be overestimated. To address this, the CCSDT(Q)/VDZ approach was utilized in the MRCC package (by Kállay *et al*. [32, 33]) for Grid_II. These calculations took from 3 to 9 hours per point, depending on the molecular symmetry.

Next, we have computed the two energy differences: [RHF-CCSD(T)-F12b/CVQZ-F12] – [RHF-CCSD(T)-F12a/VTZ-F12] and [CCSDT(Q) – CCSD(T)]/VDZ. They were summed and then fitted using expansion (1) up to the 4th order, yielding a RMS deviation of 0.03 cm^{-1}. The fitted parameters were used to predict the summed energy difference for all points of Grid_I, bringing them to the RHF-CCSD(T)-F12b/CVQZ-F12 +

CCSDT(Q)/VDZ level of the theory. The fit of the corrected energies of Grid_I yielded PES_II, with the same number of expansion coefficients and the same RMS error as PES_I.

The fundamental band origins predicted using PES_II agree with the empirical values within 1 cm^{-1}, with a RMS error of only 0.65 cm^{-1}. To our knowledge, this represents the most accurate *ab initio* description to date of the fundamentals for a "heavy" T_d-type molecule. For comparison, previous *ab initio* calculations for CF_4 [26] reproduced the ν_3 band with a discrepancy of 5 cm^{-1}, using a smaller VQZ basis set without any high-level corrections. Consequently, the present results validate the use of advanced *ab initio* methods for rigid, many-electron molecules such as SiF_4.

We should stress the fact that no scalar relativistic and DBOC corrections were included here because their contributions to the band origins are about an order of magnitude smaller than those from the high-order electronic correlations. Including such corrections is justified only when the *ab initio* energies are close to the CBS limit. As shown in Table 2, PES_II systematically underestimates all the fundamental band origins due to the lack of convergence of the *ab initio* energies with respect to the orbital basis set size. This is typical of the RHF-CCSD(T)-F12b/CVQZ-F12 approach.

Our final PES was obtained by refining the quadratic force constants of PES_II as well as the equilibrium geometry using the empirical data of Boudon *et al*. [22]. After refinement, the fundamental band origins now agree within 10^{-3} cm^{-1} while the equilibrium geometry matches within 10^{-4} Ang. (see Table 1).

3.2. DMS

The *ab initio* values of the electric dipole moment were calculated *via* the finite difference method as the first derivative of the potential energy with respect to the electric field: $\Delta V/\Delta f$. The field (f) was applied along the x axis with two magnitudes: 0.0005 and –0.0005 a.u.

In order to check convergence with respect to the orbital basis set size, two approaches were tested: RHF-CCSD(T)-F12a/AVTZ and RHF-CCSD(T)-F12b/AVQZ. As illustrated in Table 2, the first derivatives of the DMS with respect to the normal mode coordinates $q_3(F_2)$ and $q_4(F_2)$ show good convergence, with a difference between the two approaches of 0.0003 and 0.0004 Debye for $|\partial\mu/\partial q_3|$ and $|\partial\mu/\partial q_4|$, respectively. Accordingly, the less computationally demanding RHF-CCSD(T)-F12a/AVTZ approach was used to calculate the *ab initio* values of the electric dipole over the full grid of 2385 nuclear configurations. This grid covers the 6th order ITO polynomials of symmetry F_2. The final fit of the *ab initio* reference values achieved a RMS error of 10^{-5} Debye using 273 expansion parameters.

Table 2. *Ab initio* derivatives (in Debye, this work) with respect to the infrared modes q_3 and q_4 of $^{28}SiF_4$ [1]

Derivative	F12a/AVTZ	F12b/AVQZ	Empirical [2]
$\|\partial\mu/\partial q_3\|$	0.4240	0.4243	0.42 ± 0.02
$\|\partial\mu/\partial q_4\|$	0.3112	0.3108	0.30 ± 0.01

[1] The full notation of the *ab initio* method is RHF-CCSD(T)-F12x{x=a, b}.

[2] Obtained by Burtsev *et al*. [34] following the approach of Haas and Hornig [35] and by using the experimental splitting of the transverse and longitudinal optical modes (TO and LO, respectively) measured by Bernstein *et al*. [36] from the Raman spectrum of crystalline SiF_4 at 77 K.

According to Table 2, the first derivatives of our *ab initio* DMS are in an excellent agreement with the empirical results obtained by Burtsev *et al*. [34] from the Raman spectrum of crystalline SiF_4, originally measured by Bernstein *et al*. [36]. It is worth mentioning that the values of the first derivatives obtained from an empirical effective model differ from those given in Table 2. According to the recent empirical study by Boudon *et al*. [21], the effective first derivative extracted from the analysis of the line intensities of the $\nu_3(F_2)$ band was estimated as 0.5444(38) Debye. This is about 28 % larger than the present result. We suggest two main reasons to explain such a discrepancy. First, the missing hot transitions may have a significant impact on the spectrum of the gaseous SiF_4, even at lower temperatures (in particular at T=160 K, as considered in Ref. [21]), making hazardous the extraction of the line intensities of the cold bands without support of theoretical predictions. Second, only a limited number of effective dipole moment parameters was determined from analysis of the high-resolution spectra. Finally, most of the resonance interactions between the energy levels were omitted in the empirical models, leading to an incomplete set of diagonal and non-diagonal parameters. Here, the term "diagonal" refers to a parameter associated to creation and annihilation operators with the same powers. Undoubtedly, the spectral analysis using a global effective model with *ab initio*-determined parameters should provide more consistent results.

4. Effective Hamiltonian and dipole moment operator

Computing variationally the energy levels and eigenfunctions of a five-atomic, heavy molecule like SiF_4 remains a challenging task. In the previous study, the nuclear-motion problem was solved for CF_4 [26] up to J=80. In this work, higher J values are required to properly converge the integrated intensities. Within that context, a non-empirical effective model can be derived by applying a series of unitary transformations to the nuclear-motion Hamiltonian, composed of a kinetic energy operator and of the PES. As an alternative to Van Vleck, contact transformations based on perturbation theory, the novel methodology proposed in Ref. [37] was employed in this work. In this approach, instead of transforming the Hamiltonian, we search for a unitary transformation that brings selected variational eigenfunctions into a block-diagonal form, following a polyad scheme P. The corresponding matrix representation of the block-diagonal, effective Hamiltonian is thus obtained from the transformed eigenvectors and variational rotation-vibration energy levels. The key advantage of this approach in the simultaneous construction of an effective dipole moment operator.

Step 1: Variational calculation. Nuclear-motion calculations were first performed using the "rigid" version of the computer code TENSOR [38], based on the Eckart-Watson [39] ro-vibrational Hamiltonian expressed in terms of normal-mode ITOs. Both the kinetic energy and potential parts were both Taylor expanded at order 12 in terms of the nine coordinates (q_1, $q_{2(a,b)}$, $q_{3(x,y,z)}$, $q_{4(x,y,z)}$) describing the SiF_4 vibrations, before reducing the polynomial expansion at order 6, following the strategy of Ref. [38]. This strategy was already applied for computing accurate spectroscopic line lists of different semirigid molecules (for example, Refs. [40–42]), including molecules of T_d symmetry [26]. For nonrigid molecules, the "hybrid" version of the TENSOR code [43] based on the Hougen-Bunker-Johns formalism was developed and successfully applied to the quasilinear triplet CH_2 [44] as well as on the nonrigid NH_3, CH_3, and H_2O_2 molecules (see Ref. [43] and references therein).

To achieve a convergence better than 10^{-3} cm^{-1} for the vibrational levels up to 2500 cm^{-1}, 15708, 13784, 29454, 42790, and 44714 basis functions were used in the variational calculation for the symmetry blocks A_1, A_2, E, F_1, and F_2, respectively. Among all these basis functions, respectively 753, 520, 1259, 1700 and 1933 functions were selected to define reduced vibrational eigenfunctions for solving the $J > 0$ problem. Like for CF_4 or SF_6,

the normal-mode representation is very well suited for SiF_4, allowing a fast convergence of both the Hamiltonian expansion and variational calculation. It is worth mentioning that the atomic masses were employed here to approximately account for non-adiabatic effects. In this work, the rotation-vibration eigenpairs were obtained and stored up to J=15, before applying a series of transformations. Unlike DVR-like calculations, all quantum numbers are provided in a quite straightforward manner.

Step 2: Effective model. The variationally-computed eigenvector matrices characterized by J and the total symmetry C were then block diagonalized using a transformation $\mathbf{T}^{(J,C)}$ following a specific polyad scheme in order to include the most relevant resonance coupling terms. A proper characterization of all the resonance couplings is very challenging using an empirical approach, mostly due to missing information on the so-called "dark states" that may lead to poorly-defined spectroscopic parameters. This is not the case when using *ab initio* calculations which account for almost all possible resonances. In this work, an effective model was defined by following the polyad scheme $P=6\upsilon_1+2\upsilon_2+8\upsilon_3+3\upsilon_4$, up to P_{max}=19 to cover the range 0–2500 cm^{-1}. Note that the polyad number P=1 is missing using this definition so that our rotation-vibrational states will be labelled by J, C, n and P, with P=0, 2, 3, …, 19. Here, n is a ranking number sorting the energy levels in increasing order for a given (J, C, P) block. At this stage, the obtained block-diagonal Hamiltonian matrices $\mathbf{H}^{(J,C,P)}$ up to J=15 and P=19 are nothing but matrix representations of an effective Hamiltonian with a set of parameters determined through an iterative procedure (see Ref. [37]).

In this work, a global effective Hamiltonian was expanded in creation-annihilation operators up to order 14 to be able to include the band $7\nu_2$. The maximum rotational degree was 6 – except for the ground vibrational state where it was 8 – resulting in 32990 Hamiltonian parameters up to P=19. For line intensity calculations, $\mathbf{T}^{(J,C)}$ was used to transform the matrix of the dipole moment components of the laboratory-fixed frame. Finally, all $P_m - P_n$ (m=0, …, 19, n=0, …, 12) transitions were computed using 58594 ITOs of symmetry F_2.

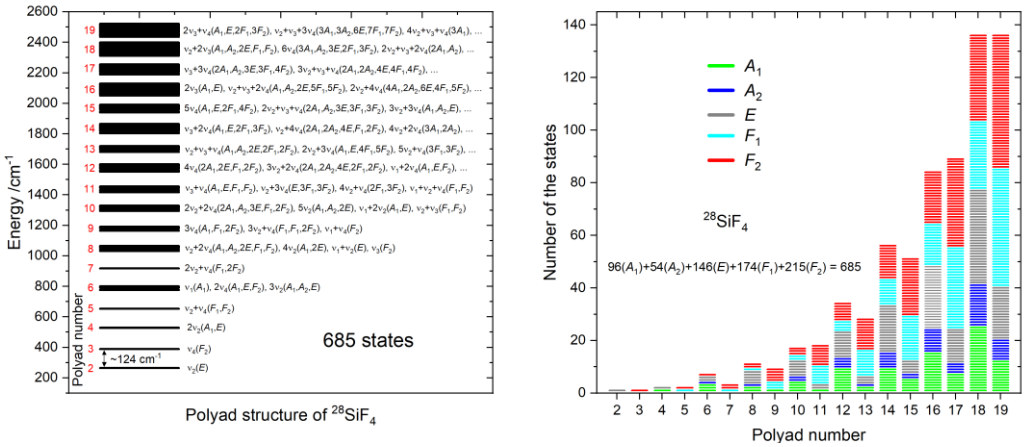

Figure 2. Polyad structure of the vibrational states of $^{28}SiF_4$: energy scale (left panel); symmetries of the states inside each polyad (right panel).

The polyad structure of $^{28}SiF_4$ obtained in this work is depicted in Figure 2 (left panel). A total of 685 excited vibrational sub-states was computed using this scheme. The energy gap between the lowest polyad is about 124 cm^{-1}, but it decreases gradually for higher polyads which include much more vibrational states. For example, each of the last two polyads, namely P=18 and P=19, contains 136 vibrational sub-states (Figure 2, right panel). A similar polyad scheme was applied for $^{29}SiF_4$ and $^{30}SiF_4$.

Finally, more than 95 % of the vibrational band and sub-bands produced by our effective model have been never empirically studied so far. All these states led to a tremendous number of hot transitions, required for converging the opacity at T=296 K.

5. Partition function

To estimate the maximum value J_{max} for each polyad as well as the population of a rovibrational state at a given temperature (T), we can compute the partition function

$$Q(T) = \sum_j g_j \exp\left(-\frac{h \cdot c \cdot E_j}{k_B T}\right), \quad (6)$$

where h [J×s] and k_B [J×K^{-1}] are the Planck and Boltzmann constants; c is the speed of light [cm×s^{-1}]; g_j is the statistical weight of the energy level E_j [cm^{-1}]. The total statistical weight is given by g=g_{ev} g_{rot}, where g_{ev} corresponds to the electronic and vibrational degeneracies, while the rotational part g_{rot} is the product of the (2·J + 1) degeneracy in the absence of an external electromagnetic field with the nuclear spin statistical weight.

For the main isotopologue $^{28}SiF_4$ the nuclear spins of the atoms are $I(^{28}Si)$=0 and $I(^{19}F)$=1/2. Thus, $^{28}SiF_4$ has the same nuclear statistical weights as those of $^{12}CH_4$, namely 5, 5, 2, 3, and 3 for the A_1, A_2, E, F_1, and F_2 symmetries of the T_d point group. $^{30}SiF_4$ has the same weights since $I(^{30}Si)$=0. The case of the $^{29}SiF_4$ isotopologue is different because of $I(^{29}Si)$=1/2 leading to a state independent weight of 2. However, the state independent weight does not change the line intensity, and therefore will be omitted.

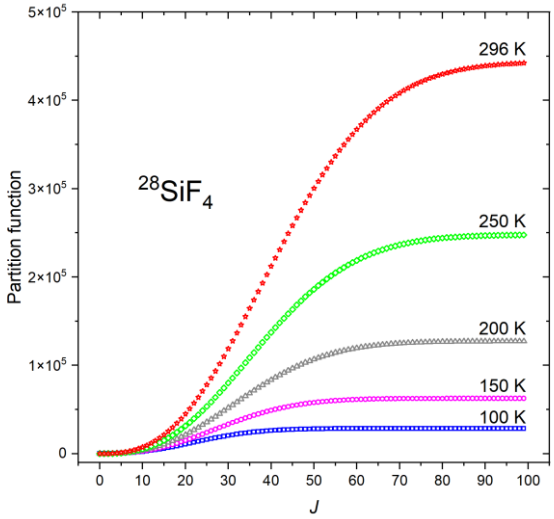

Figure 3. Convergence of the partition sum of $^{28}SiF_4$ at different temperatures.

Equation (6) was summed over 4826347 energy levels computed from our new effective Hamiltonian. From the *direct* sum (6), the partition function of $^{28}SiF_4$ is of 442170. Using the product approximation $Q = Q_{rot}Q_{vib}$, the value of the partition function differs by 0.5 %, as 440028. This approximation is used when a full set of energy levels is not available, in particular, in the HITRAN database (see Gamache *et al.* [45]). For the two other isotopologues, the direct sum (6) gives 444226 ($^{29}SiF_4$) and 446257 ($^{30}SiF_4$), which are close within 0.46 % and 0.92 % to that of $^{28}SiF_4$.

As shown in Figure 3, the partition function is converged for energy levels up to J=60 for the temperature range (T=100–150 K). At room temperature (296 K), the difference between J=98 and J=99 is below 0.05 %, so that J_{max}=99 was considered in this study.

6. Cut-off values and super-lines

Selecting appropriate cut-off values for line intensities and angular momentum J for each polyad of SiF_4 can be a tricky task due to the huge number of the transitions. At a fixed intensity cut-off, the number of transitions may change significantly, even by incrementing J.

The intensities [cm^{-1}/(molecule·cm^{-2})] of the ro-vibrational transitions were computed using the following formula

$$I_{f\leftarrow i} = \frac{8\cdot\pi^3\cdot\nu_{if}}{3\cdot h\cdot c\cdot Q(T)}\cdot g_i\cdot\exp\left(-\frac{h\cdot c\cdot E_i}{k_B\cdot T}\right)\cdot\left(1-\exp\left(-\frac{h\cdot c\cdot\nu_{if}}{k_B\cdot T}\right)\right)\cdot S(f\leftarrow i), \quad (7)$$

where the subscripts f and i refer to the final (upper) and initial (lower) states; ν_{if} [cm^{-1}] is the line position, $\nu_{if} = E_f - E_i$; other definitions are explained in Equation (6). The square of the matrix element of the molecular electric dipole moment known as the line strength (see, *e.g.*, Bunker and Jensen [46]), $S(f\leftarrow i)$, was computed using the *ab initio* eigenfunctions of the effective Hamiltonian as well as the components of the dipole moment.

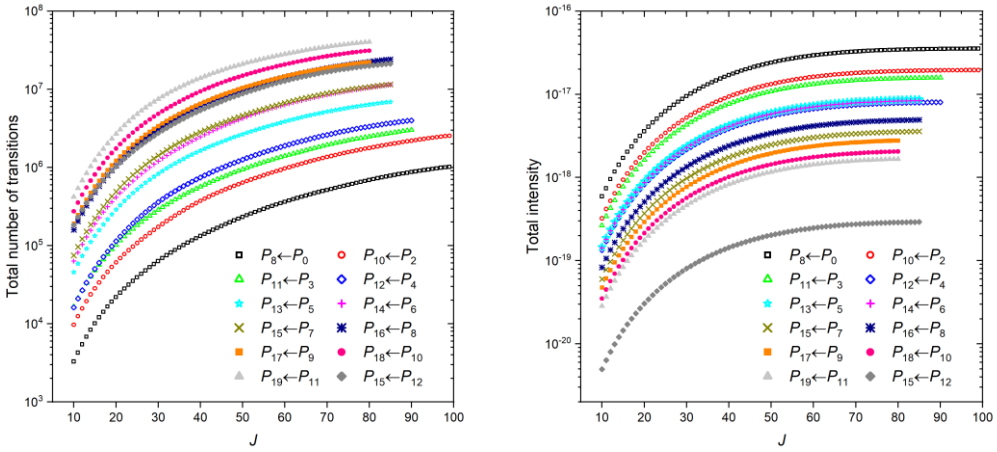

Figure 4. Number of the $P_m\leftarrow P_n$ transitions as a function of J (left panel). Convergence of the total intensity at T=296 K for different $P_m\leftarrow P_n$ transitions (right panel).

The energy levels and transitions were computed up to J_{max}=99 for the first ten polyads, namely, P=0 and P=2-10. Above, the J_{max} value was gradually decreased, namely from J_{max}=90 (P=11, 12), 85 (P=13–16) to 80 (P=17–19). The polyad transitions with the highest numbers of lines are displayed in Figure 4 (left panel). In terms of lines, the cold bands are dominated by $P_8\leftarrow P_0$ composed of about $\approx 10^6$ lines, while the hot $P_{19}\leftarrow P_{11}$ is composed of about $\approx 4\times 10^7$ lines. As indicated by the polyad structure given in Figure 2, both types of interpolyad transitions are characterized by $\Delta\upsilon_3=\pm 1$, which corresponds to the strongest dipole derivative with respect to the normal coordinate q_3 in SiF_4 (see Table 2).

The total intensity of the transitions follows a Boltzmann distribution (Figure 4, right panel), meaning that the contribution of the hot transitions depends on the energy of the lower polyad. For that reason, the $P_{10}\leftarrow P_2$ and $P_{11}\leftarrow P_3$ hot transitions rank second and third, just after $P_8\leftarrow P_0$. Interestingly, the combined absorption for these two hot transitions is comparable to that of the cold one, with intensities of 3.533×10^{-17} and 3.526×10^{-17} cm^{-1}/(molecule·cm^{-2}) (hereafter, cm/molecule), respectively.

Figure 4 also illustrates a typical difficulty when constructing line lists of "heavy" molecules: a large number of hot transitions (*e.g.*, $P_{18}\leftarrow P_{10}$ or $P_{19}\leftarrow P_{11}$) composed mainly of weak lines is involved. Actually, such transitions form a quasi-continuum absorption

background which is not resolved because of the high density of lines, but cannot be ignored for proper opacity calculations, in particular, at room temperature.

Following the strategy previously established, in particular for CF_4 [26] and SF_6 [41] in order to make fast spectra simulations, we have defined so-called "strong" and "weak" lines. In this approach, it was suggested to model the quasi-continuum formed by the contributions of huge amounts of very weak lines using so-called "super-lines", which represent integrated intensity contributions on a pre-defined grid of small wavenumber and temperature intervals. The initial line list for $^{28}SiF_4$ – computed using a cut-off of 10^{-30} cm/molecule for rotational transitions and of 10^{-28} cm/molecule otherwise – contained nearly half a billion transitions (448,594,361) over the range [0–2500] cm^{-1}. This list was subsequently reduced to 18,477,082 "strong" lines by applying a cutoff of 10^{-25} cm/molecule. The list composed by only "strong" lines covers the range [0–2100] cm^{-1} while the remaining transitions were converted to super-lines using a 10^{-3} cm^{-1} step size. The line list for $^{29}SiF_4$ and $^{30}SiF_4$ contain similar numbers of the transitions, as the isotopic abundance was fixed to 100 % for all species.

7. Validation

7.1. General comments

The experimental PNNL spectrum of SiF_4 contains various impurities resulting from its hydrolysis. Among these, SiF_3OSiF_3 (hereafter, Si_2F_6O) is the most thermodynamically favorable product [4]. The presence of Si_2F_6O was noted in both early and recent experimental studies (see, *e.g.*, Refs. [14, 22, 23]). As it will be demonstrated in this section, the contribution of Si_2F_6O in the PNNL cross-sections (measured at 298 K) is comparable in magnitude to some combination, overtone and hot bands of SiF_4.

The absorption cross-sections of the natural SiF_4 were simulated using the line lists of all three isotopologues. To this end, the line intensities were scaled by the following natural abundancies: 0.92223, 0.04685, and 0.03092 for $^{28}SiF_4$, $^{29}SiF_4$, and $^{30}SiF_4$, respectively. A Lorentzian line profile with a constant half-width at half-maximum (HWHM) of 0.05 cm^{-1} was applied. The spectral step was set to 0.06 cm^{-1} and the simulation was made at a temperature of 296 K.

Table 3. Integrated intensities of the strongest bands of $^{28}SiF_4$ displayed in Figure 5. [1]

Origin (cm^{-1})	Band	Region (cm^{-1})	*N*	I_v(cm / molecule)	
				This work	TFSiCaSDa
	(0010)–(0010)(F_2)	1–57	58547	6.363×10^{-24}	
	(0000)–(0000)(A_1)	5–28	9055	1.540×10^{-24}	
	(0110)–(0110)(F_2)	2–57	23864	1.142×10^{-24}	
	(0110)–(0110)(F_1)	2–57	21379	1.087×10^{-24}	
124.175	$\nu_2+\nu_4(F_1)-2\nu_2(E)$	111–144	1444	2.015×10^{-23}	
124.214	$\nu_4(F_2)-\nu_2(E)$	106–147	11554	2.650×10^{-22}	
124.426	$\nu_2+\nu_4(F_2)-2\nu_2(E)$	109–139	1797	2.304×10^{-23}	
125.907	$\nu_2+\nu_4(F_2)-2\nu_2(A_1)$	111–145	3331	4.536×10^{-23}	
263.204	$2\nu_2(A_1)-\nu_2(E)$	240–286	4290	1.408×10^{-21}	
263.669	$3\nu_2(E)-2\nu_2(A_1)$	243–284	1590	4.030×10^{-22}	
264.219	$\nu_2(E)$	236–290	9570	5.559×10^{-21}	
264.646	$\nu_2+\nu_4(F_1)-\nu_4(F_2)$	243–285	1739	4.123×10^{-22}	
264.685	$2\nu_2(E)-\nu_2(E)$	239–289	3746	1.168×10^{-21}	

264.897	$\nu_2+\nu_4(F_2)-\nu_4(F_2)$	244–285	2193	5.396×10^{-22}	
387.522	$2\nu_4(A_1)-\nu_4(F_2)$	359–418	99620	6.361×10^{-19}	
388.433	$\nu_4(F_2)$	361–419	62659	6.155×10^{-18}	5.775×10^{-18}
388.633	$2\nu_4(F_2)-\nu_4(F_2)$	361–420	163332	1.894×10^{-18}	
388.860	$\nu_2+\nu_4(F_1)-\nu_2(E)$	361–419	69260	1.353×10^{-18}	
389.025	$2\nu_4(E)-\nu_4(F_2)$	361–422	97931	1.132×10^{-18}	
389.111	$\nu_2+\nu_4(F_2)-\nu_2(E)$	362–419	86260	2.056×10^{-18}	
389.536	$2\nu_2+\nu_4(F_1)-2\nu_2(E)$	362–420	97970	4.352×10^{-19}	
389.576	$2\nu_2+\nu_4(F_2)-2\nu_2(E)$	362–420	117984	4.933×10^{-19}	
391.057	$2\nu_2+\nu_4(F_2)-2\nu_2(A_1)$	362–420	43194	4.553×10^{-19}	
640.597	$\nu_2+\nu_3(F_2)-\nu_2+\nu_4(F_2)$	610–663	2118	2.864×10^{-23}	
640.848	$\nu_2+\nu_3(F_2)-\nu_2+\nu_4(F_1)$	608–665	2713	4.091×10^{-23}	
642.119	$\nu_2+\nu_3(F_1)-\nu_2+\nu_4(F_2)$	612–665	2447	3.172×10^{-23}	
642.370	$\nu_2+\nu_3(F_1)-\nu_2+\nu_4(F_1)$	610–663	1579	2.206×10^{-23}	
643.111	$\nu_3(F_2)-\nu_4(F_2)$	602–672	18227	4.499×10^{-22}	
653.330	$\nu_2+\nu_4(F_2)$	639–672	2825	3.494×10^{-23}	
766.504	$\nu_2+\nu_3(F_2)-2\nu_2(A_1)$	741–798	2937	7.475×10^{-22}	
767.325	$\nu_3(F_2)-\nu_2(E)$	737–803	11353	4.964×10^{-21}	
777.066	$2\nu_4(F_2)$	758–802	9678	5.829×10^{-21}	
777.458	$2\nu_4(E)$	760–800	3184	1.339×10^{-21}	
777.856	$3\nu_4(F_1)-\nu_4(F_2)$	761–798	3723	1.043×10^{-21}	
778.296	$\nu_2+2\nu_4(F_1)-\nu_2(E)$	763–799	3151	8.519×10^{-22}	
1028.973	$\nu_3+\nu_4(E)-\nu_4(F_2)$	998–1062	58012	2.899×10^{-18}	2.477×10^{-18}
1029.400	$2\nu_2+\nu_3(F_1)-2\nu_2(E)$	996–1060	113020	2.301×10^{-18}	
1029.708	$\nu_2+\nu_3(F_2)-\nu_2(E)$	991–1065	85877	9.991×10^{-18}	1.116×10^{-17}
1030.174	$\nu_3+\nu_4(F_2)-\nu_4(F_2)$	997–1060	63366	3.541×10^{-18}	5.420×10^{-18}
1030.341	$2\nu_2+\nu_3(F_2)-2\nu_2(E)$	993–1063	211923	3.007×10^{-18}	
1030.445	$\nu_3+\nu_4(F_1)-\nu_4(F_2)$	992–1064	121231	6.275×10^{-18}	7.309×10^{-18}
1031.031	$\nu_3+\nu_4(A_1)-\nu_4(F_2)$	1000–1062	63240	3.031×10^{-18}	1.624×10^{-18}
1031.230	$\nu_2+\nu_3(F_1)-\nu_2(E)$	988–1068	88859	9.425×10^{-18}	9.985×10^{-18}
1031.544	$\nu_3(F_2)$	987–1068	53957	3.491×10^{-17}	3.860×10^{-17}
1031.822	$2\nu_2+\nu_3(F_2)-2\nu_2(A_1)$	995–1064	56483	2.460×10^{-18}	
1051.287	$\nu_1+\nu_3(F_2)-2\nu_4(F_2)$	1014–1038	1226	2.464×10^{-21}	
1063.382	$\nu_1+2\nu_2(A_1)-\nu_2(E)$	1033–1083	7167	3.339×10^{-21}	
1064.650	$\nu_1+\nu_2(E)$	1034–1088	12965	1.183×10^{-20}	
1064.982	$\nu_1+2\nu_2(E)-\nu_2(E)$	1035–1086	8762	2.862×10^{-21}	
1066.009	$\nu_1+\nu_2+\nu_4(F_1)-\nu_4(F_2)$	1039–1083	3588	1.002×10^{-21}	
1066.292	$\nu_1+\nu_2+\nu_4(F_2)-\nu_4(F_2)$	1039–1083	4119	1.252×10^{-21}	
1166.658	$3\nu_4(F_2)$	1140–1192	13478	1.793×10^{-20}	
1190.005	$\nu_1+\nu_4(F_2)$	1161–1219	22899	1.311×10^{-19}	
1190.223	$\nu_1+\nu_2+\nu_4(F_1)-\nu_2(E)$	1164–1217	18203	3.133×10^{-20}	
1190.506	$\nu_1+\nu_2+\nu_4(F_2)-\nu_2(E)$	1164–1217	20531	3.533×10^{-20}	
1191.034	$\nu_1+2\nu_4(F_2)-\nu_4(F_2)$	1165–1217	28004	3.722×10^{-20}	
1293.927	$\nu_2+\nu_3(F_2)$	1248–1332	25760	7.186×10^{-20}	

1294.085	$2\nu_2+\nu_3(F_1)-\nu_2(E)$	1253–1326	24701	2.108×10^{-20}
1294.790	$\nu_2+\nu_3+\nu_4(F_2)-\nu_4(F_2)$	1255–1326	20682	1.084×10^{-20}
1294.892	$\nu_2+\nu_3+\nu_4(F_1)-\nu_4(F_2)$	1254–1326	18596	1.070×10^{-20}
1295.026	$2\nu_2+\nu_3(F_2)-\nu_2(E)$	1251–1329	49899	5.538×10^{-20}
1295.449	$\nu_2+\nu_3(F_1)$	1248–1329	20422	2.746×10^{-20}
1417.406	$\nu_3+\nu_4(E)$	1381–1439	7620	3.130×10^{-22}
1418.607	$\nu_3+\nu_4(F_2)$	1380–1441	9590	9.213×10^{-22}
1418.752	$\nu_3+2\nu_4(F_2)-\nu_4(F_2)$	1388–1448	14347	2.304×10^{-22}
1418.878	$\nu_3+\nu_4(F_1)$	1392–1443	12166	4.422×10^{-22}
1419.106	$\nu_2+\nu_3+\nu_4(F_1)-\nu_2(E)$	1381–1439	10396	3.187×10^{-22}
1439.920	$\nu_1+\nu_3(F_2)-\nu_4(F_2)$	1415–1462	1888	2.241×10^{-23}
1454.442	$\nu_1+\nu_2+\nu_4(F_1)$	1442–1471	488	5.751×10^{-24}
1454.725	$\nu_1+\nu_2+\nu_4(F_2)$	1440–1472	3899	6.313×10^{-23}
1455.529	$\nu_1+2\nu_2+\nu_4(F_1)-\nu_2(E)$	1455–1470	219	2.253×10^{-24}
1455.577	$\nu_1+2\nu_2+\nu_4(F_2)-\nu_2(E)$	1444–1467	245	2.446×10^{-24}
1806.026	$\nu_3+3\nu_4(F_1)-\nu_4(F_2)$	1795–1836	2380	5.649×10^{-22}
1806.819	$\nu_3+3\nu_4(F_2)-\nu_4(F_2)$	1795–1836	1976	4.870×10^{-22}
1807.185	$\nu_3+2\nu_4(F_2)$	1794–1837	8204	4.868×10^{-21}
1807.384	$\nu_2+\nu_3+2\nu_4(F_1)-\nu_2(E)$	1796–1837	2632	7.460×10^{-22}
1807.462	$\nu_2+\nu_3+2\nu_4(F_2)-\nu_2(E)$	1796–1835	3543	1.126×10^{-21}
1826.312	$\nu_1+\nu_2+\nu_3(F_2)-\nu_2(E)$	1812–1836	11704	2.802×10^{-20}
1827.820	$\nu_1+\nu_2+\nu_3(F_1)-\nu_2(E)$	1812–1836	10932	2.649×10^{-20}
1827.939	$\nu_1+\nu_3+\nu_4(F_2)-\nu_4(F_2)$	1814–1837	8106	9.321×10^{-21}
1828.179	$\nu_1+\nu_3+\nu_4(F_1)-\nu_4(F_2)$	1814–1837	14154	1.621×10^{-20}
1828.353	$\nu_1+\nu_3(F_2)$	1814–1837	10252	1.050×10^{-19}
1990.540	$2\nu_1+\nu_4(F_2)$	1975–2006	1641	3.350×10^{-22}
2056.109	$\nu_2+2\nu_3(F_1)-\nu_2(E)$	2009–2098	16402	1.632×10^{-20}
2057.601	$\nu_2+2\nu_3(F_2)-\nu_2(E)$	2009–2098	14291	1.378×10^{-20}
2059.017	$2\nu_3(F_2)$	2007–2106	21440	5.804×10^{-20}
2060.395	$2\nu_3+\nu_4(F_2)-\nu_4(F_2)$	2008–2098	22522	1.007×10^{-20}
2060.865	$2\nu_3+\nu_4(F_1)-\nu_4(F_2)$	2008–2097	22779	1.145×10^{-20}
2063.332	$2\nu_3(E)$	2008–2107	17304	2.371×10^{-20}

[1] The integrated intensities are the sum of the intensities of the ro-vibrational lines for a given band at T=296 K. The isotopic abundancy is not included. For further description of the TFSiCaSDa line list, see Richard *et al*. [24].

Table 3 gives the integrated intensities of the bands contributing significantly to the absorption, as displayed in Figure 5. As a comparison, the simulation based on the empirical TFSiCaSDa line list is also provided. According to Ref. [24], the TFSiCaSDa line list includes the transitions for the two fundamental bands, $\nu_4(F_2)$ and $\nu_3(F_2)$, as well as for several hot bands associated with $\Delta\upsilon_3=\pm1$. The line intensities for these hot bands were calculated using empirical dipole moment parameters derived from $\nu_3(F_2)$ and obtained in Ref. [21] from the analysis of individual line strengths. For the $\nu_4(F_2)$ band, the vibrational transition moment was estimated from the measured integrated intensity in Ref. [22].

The line lists developed in this work were based on a global *ab initio* approach accounting for almost all resonance interactions in a given polyad P (Figure 2). Moreover, a complete set of effective dipole moment parameters describing both cold and hot band transitions was derived from our *ab initio* DMS.

7.2. Region: 0–300 cm^{-1}

SiF_4 being a spherical top molecule, its rotational spectrum is mainly induced by centrifugal distortion. As shown in Table 3 and Figure 5A, the rotational transitions within the excited (0010) state are the strongest (~6×10^{-24} cm/molecule), which is consistent with the high-resolution measurements by Takami and Kuze [18]. The rotational transitions within the ground vibrational states are much weaker [20].

The hot $\nu_4(F_2)$–$\nu_2(E)$ band located at 124 cm^{-1} also falls in this region (see Figure 5B). This hot band was clearly observed in the FTIR spectrum recorded at low temperature (160 K) by Boudon *et al*. [22], leading a detailed analysis of its line positions. Up to our knowledge, the line intensities, however, have not been empirically studied yet. As shown in Table 3, the integrated intensity of $\nu_4(F_2)$–$\nu_2(E)$ is about two orders of magnitude greater than that of the rotational bands.

The fundamental $\nu_2(E)$ band located at 264 cm^{-1} (see Figure 5C) is not infrared active, unlike in the Raman spectrum of SiF_4 (see, *e.g.*, Clark and Rippon [47]). There is no first derivative of the electric DMS with respect to the normal mode coordinate $q_2(E)$. Consequently, the transition moment is governed by higher-order, rotational-dependent terms in the expansion of the effective dipole moment. Nevertheless, the absorption in this spectral region is stronger. The integrated intensity of $\nu_2(E)$ is of order 10^{-21} cm/molecule, similar to that of the two hot bands: $2\nu_2(E)$–$\nu_2(E)$ and $2\nu_2(A_1)$–$\nu_2(E)$ (see Table 3).

7.3. Region of $\nu_4(F_2)$

The sum of intensities of the hot bands associated with $\Delta\upsilon_4=\pm1$ is larger than that of the fundamental $\nu_4(F_2)$ band located at 388 cm^{-1}. As a result, the position of the total absorption peak is slightly shifted to the right from the origin of the $\nu_4(F_2)$ band. This is clearly seen when compared to the simulation based on the TFSiCaSDa line list where such hot bands are missing (see Figure 5D). The integrated intensity of $\nu_4(F_2)$ is 6 % smaller in TFSiCaSDa compared to this work (see Table 3). The effective value of 0.3706 Debye for the first derivative of the DMS with respect to $q_4(F_2)$ obtained in Ref. [22] without analysis of the individual line strength (*i.e.*, under the zero-order approximation) is, on the contrary, 19 % larger than the *ab initio*-based derivative obtained in this work (Table 2). This discrepancy may be explained by the zero-order approximation considered in Ref. [22].

In addition, there are other types of hot bands in the right wing of $\nu_4(F_2)$. Among these, we can mention the strongest one, namely $\nu_1(A_1)$–$\nu_4(F_2)$, located at 412 cm^{-1}. It was considered in Ref. [22] in order to help for the determination of the effective parameters of the fundamental $\nu_1(A_1)$ band. According to our line list, the integrated intensity of the $\nu_1(A_1)$–$\nu_4(F_2)$ hot band is about two orders of magnitude smaller than that of the fundamental $\nu_4(F_2)$ band, making it not visible in Figure 5D.

7.4. Region: 570–880 cm^{-1}

The hot bands with $\Delta\upsilon_3=\Delta\upsilon_4=\pm1$ give the main contribution to the absorption in the spectral region at 643 cm^{-1} (see Figure 5E). This region also includes the combination band $\nu_2+\nu_4$ located at 653 cm^{-1} that consists of the two sub-bands, namely, $\nu_2+\nu_4(F_1)$ and $\nu_2+\nu_4(F_2)$ analyzed in Ref. [23]. However, the F_1 sub-band is rather weak, while the integrated intensity of the F_2 sub-band is one order of magnitude smaller than that of the $\nu_3(F_2)$–$\nu_4(F_2)$ hot band (see Table 3).

The $2\nu_4(E)$ and $2\nu_4(F_2)$ bands are responsible for the prominent absorption peak at 777 cm^{-1}. Another peak at 767 cm^{-1} is mainly caused by the $\nu_3(F_2)$–$\nu_2(E)$ hot band. The line intensities of the fundamental $\nu_1(A_1)$ band at 800 cm^{-1} were too weak to include in the list of strong lines. For this reason, the $\nu_1(A_1)$ transitions were directly converted to super-lines. The strongest absorption peak at 840 cm^{-1} presented in PNNL originates from the antisymmetric Si-F stretching mode of Si_2F_6O. From Figure 5F, we can see that the maximum of the absorption due to Si_2F_6O is about two times larger than that of SiF_4.

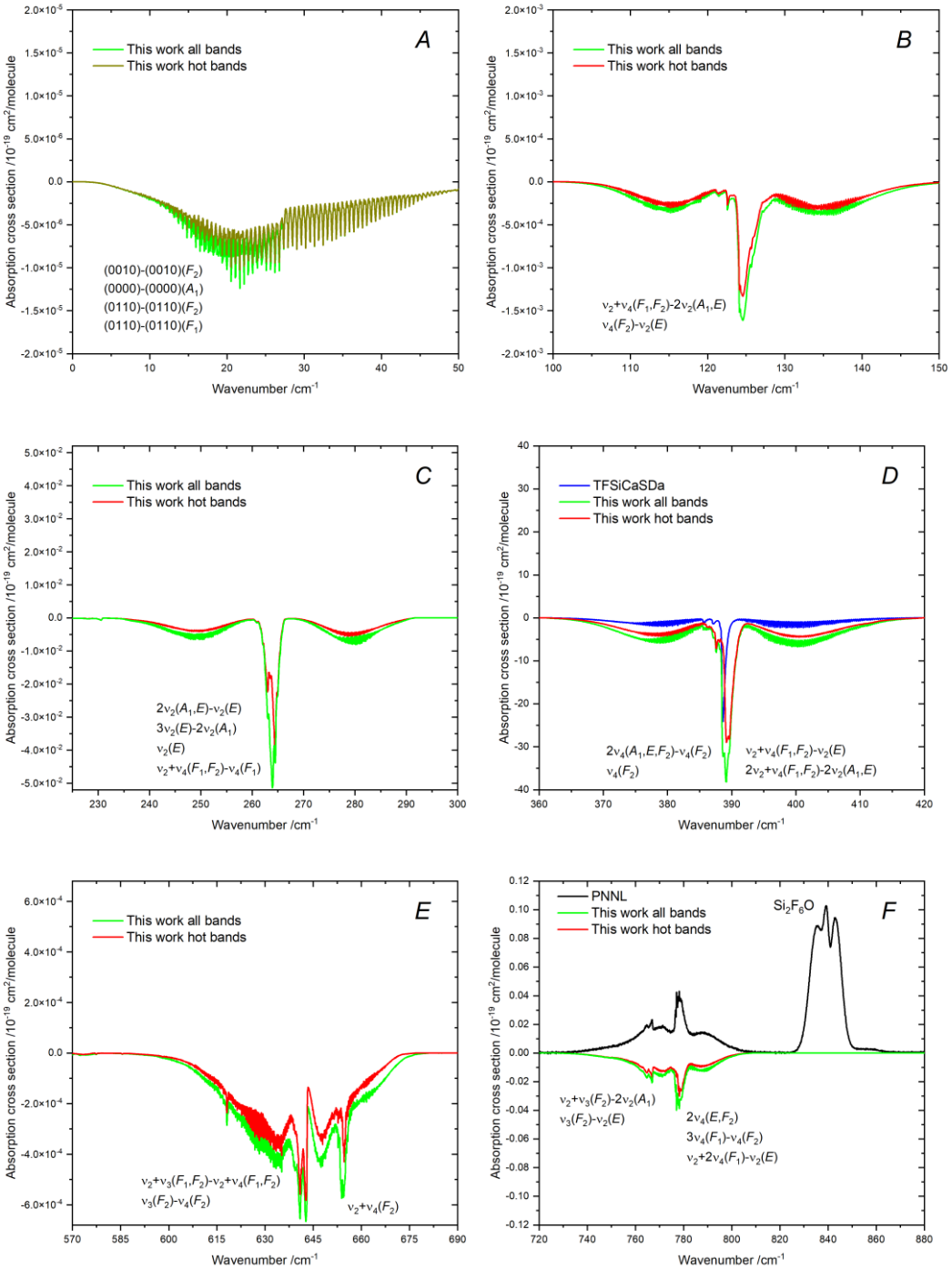

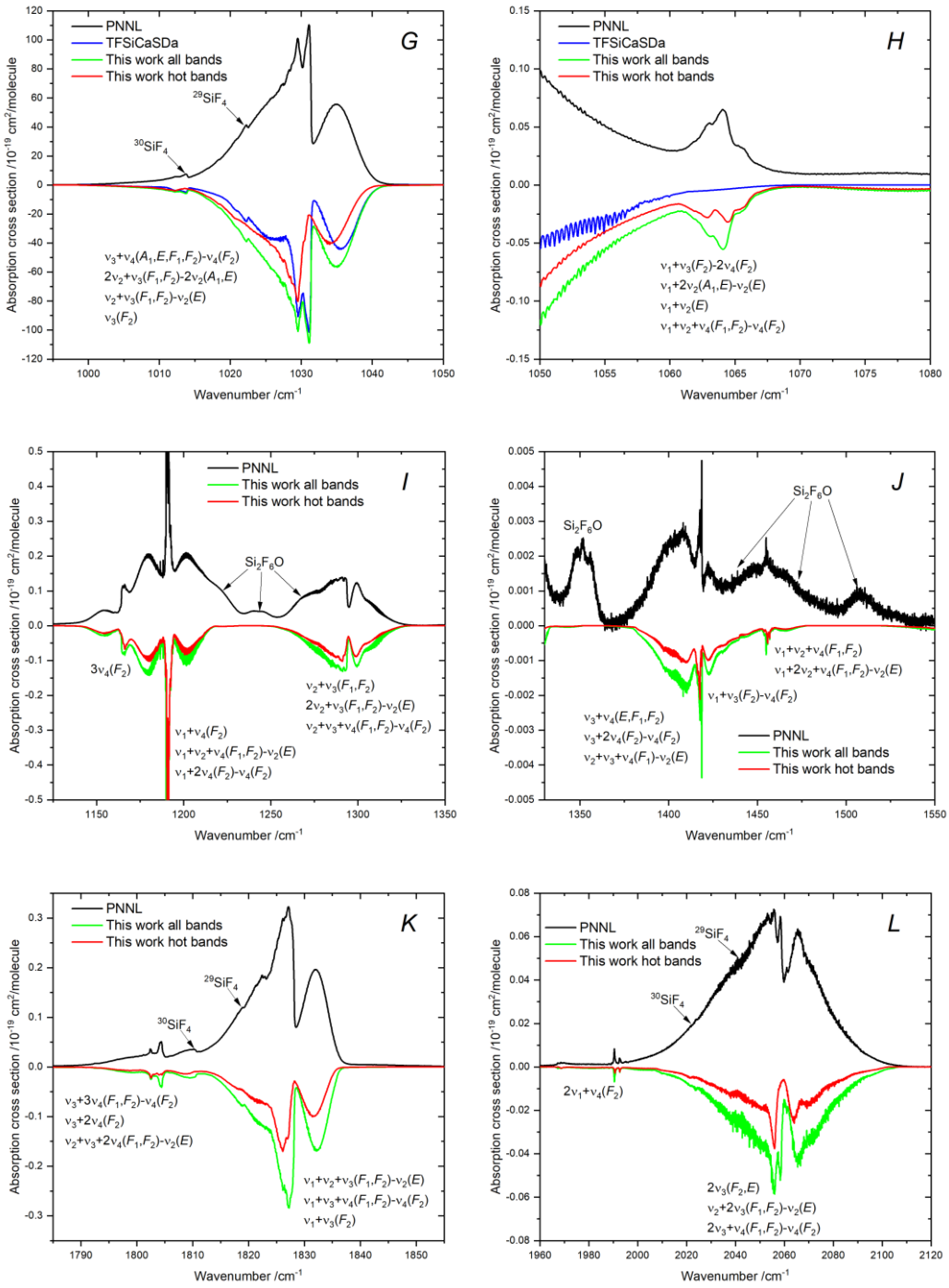

Figure 5. Absorption cross-sections of the natural silicon tetrafluoride ($^{28}SiF_4$, $^{29}SiF_4$, and $^{30}SiF_4$ isotopologues are included) simulated using this work line lists in comparison with the observed data after 700 cm^{-1} (PNNL [25]). The vibrational assignment of the dominant bands is given (their integrated intensities are presented in Table 3). The absorption due to Si_2F_6O is displayed

7.5. Region of $\nu_3(F_2)$

Figure 5G displays the most famous spectral region of SiF_4 corresponding to the strongest fundamental band $\nu_3(F_2)$. The integrated intensity of $\nu_3(F_2)$ presented in TFSiCaSDa is 11 % larger than the present *ab initio* result (see Table 3). The results on $\nu_3(F_2)$ in TFSiCaSDa were probably biased by missing hot bands. According to Ref. [21], the effective value of the first derivative of the DMS with respect to $q_3(F_2)$ was of 0.5444(38) Debye. It is 28 % larger than the *ab initio* value given in Table 2. Although, the effective

derivative cannot be directly compared with the *ab initio* one for different reasons (in particular, because data in Table 2 corresponds to the pure vibrational task, *i.e.*, the contribution from the rotational operators is not included), we assume that the line intensities of $\nu_3(F_2)$ are slightly overestimated in TFSiCaSDa due to numerous hot transitions, which could not be accurately removed without support of *ab initio* predictions.

The integrated intensities of the hot bands presented in TFSiCaSDa, namely $\nu_3+\nu_4(A_1, E, F_1, F_2)-\nu_4(F_2)$ and $\nu_2+\nu_3(F_1, F_2)-\nu_2(E)$, differ from this work by 25 % in average: the maximum difference is of 53 % [$\nu_3+\nu_4(F_2)-\nu_4(F_2)$], while the minimum difference is of 6 % [$\nu_2+\nu_3(F_1)-\nu_2(E)$] (see Table 3). Interestingly, the total integrated intensity of those hot bands is only 8 % larger than that obtained from the present line list. Nevertheless, the simulations based on the TFSiCaSDa line list underestimate the experiment, particularly in the left and right wings of $\nu_3(F_2)$ (see Figure 5G), mainly due to the absence of other hot bands, relevant at T=296 K.

7.6. Region: 1050–1550 cm^{-1}

The first part of this region corresponds to the $\nu_1+\nu_2(E)$ combination band located around 1065 cm^{-1}. Although the integrated intensity of $\nu_1+\nu_2(E)$ is of order 10^{-20} cm/molecule, this band is clearly seen in the PNNL spectrum (see Figure 5H). Note that the line positions of $\nu_1+\nu_2(E)$ have been not empirically studied so far because of their overlapping with the right wing of the strongest $\nu_3(F_2)$ band. There are hot bands with $\Delta\upsilon_1=\Delta\upsilon_2=\pm1$ and the hot band $\nu_1+\nu_3(F_2)-2\nu_4(F_2)$ at 1051 cm^{-1}; their integrated intensities are comparable (see Table 3).

Between 1167 and 1190 cm^{-1}, there are two cold bands, namely, $3\nu_4(F_2)$ and $\nu_1+\nu_4(F_2)$ (see Figure 5I). Quite surprisingly, the $3\nu_4(F_2)$ band is stronger than $2\nu_4(F_2)$ band, while $\nu_1+\nu_4(F_2)$ is the strongest combination band of SiF_4. The second absorption peak around 1295 cm^{-1} originates from the F_1 and F_2 sub-bands of the combination band $\nu_2+\nu_3$. The integrated intensity of the F_2 sub-band is about 2.5 times larger than that of the first one.

The empirical line positions of $\nu_1+\nu_4(F_2)$ and $\nu_2+\nu_3(F_1, F_2)$ were previously assigned in Ref. [23], based on spectra recorded at low temperature. However, those two bands alone are not sufficient to completely describe the absorption features observed in the room-temperature spectrum. Indeed, as seen in Table 3, the total absorption of the cold and hot bands becomes comparable at room temperature.

The absorption coefficient simulated using our line list shows a good agreement with the experimental measurements, except for several distinct absorption features (see Figure 5I). The unexplained feature observed between $\nu_1+\nu_4(F_2)$ and $\nu_2+\nu_3(F_1, F_2)$ and located at 1243 cm^{-1} is likely caused by the antisymmetric Si-O stretching mode of Si_2F_6O. Other unexplained features clearly observed in the wings of the SiF_4 bands are most likely due to the combination or overtone bands of Si_2F_6O. Indeed, this hypothesis comes from the fact that many of the fundamental frequencies of Si_2F_6O are below 1000 cm^{-1}.

The two peaks in the last part of this spectral region correspond to $\nu_3+\nu_4$ and $\nu_1+\nu_2+\nu_4$, at 1419 and 1455 cm^{-1}, respectively. These two bands are rather weak and appear to be significantly perturbed in the PNNL spectrum (see Figure 5J). The remaining unexplained absorption features may be assigned to combination or overtone bands of Si_2F_6O, considering its previously established contribution (see, *e.g.*, Figure 5F). The $\nu_3+\nu_4$ band consists of the four sub-bands corresponding to the A_1, E, F_1, and F_2 symmetries, while there are the F_1 and F_2 sub-bands in the $\nu_1+\nu_2+\nu_4$ band. In both cases, the strongest transitions belong to the F_2 sub-bands, as expected. Currently, no high-resolution studies have been reported for these bands.

7.7. Region: 1790–2120 cm^{-1}

The $\nu_1+\nu_3(F_2)$ band at 1828 cm^{-1} is the second strongest combination band of SiF_4, just after $\nu_1+\nu_4(F_2)$. Some absorption features due to $^{29}SiF_4$ and $^{30}SiF_4$ are clearly visible in the left wing of $\nu_1+\nu_3(F_2)$, similarly to the $\nu_3(F_2)$ band (see Figure 5K). The $\upsilon_3(F_2)$ mode has the largest isotopic shift among other fundamentals, respectively of –9 and –17 cm^{-1} for $^{29}SiF_4$ and $^{30}SiF_4$. These pronounced shifts facilitate the study of the line parameters of the minor isotopologues, when υ_3 is involved. For instance, the empirical line positions of the $\nu_1+\nu_3(F_2)$ band were assigned in Ref. [23] for all three isotopologues. Note that $\nu_3+2\nu_4$ exhibits a noticeable absorption feature at the lower edge of $\nu_1+\nu_3(F_2)$.

The two sub-bands $2\nu_3(E, F_2)$ are responsible for the last prominent absorption peak of SiF_4 at 2060 cm^{-1} (see Figure 5L). The absorption features due to $^{29}SiF_4$ and $^{30}SiF_4$ are less pronounced in the left wing of this band due to overlap with the nearby hot bands. As shown in Table 3, the integrated intensities of the hot bands are comparable to that of $2\nu_3$, unlike in the region of the $\nu_1+\nu_3(F_2)$ band.

The simulations based on the line list developed in this work show a good agreement with PNNL in the regions of $\nu_1+\nu_3(F_2)$ and $2\nu_3(E, F_2)$. However, some absorption features are still absent in our simulations. The first one is the small peak located inside the $\nu_1+\nu_3(F_2)$ band at 1822.5 cm^{-1}. The simulated absorption is below the observation around 1837 cm^{-1}. In the case of the $2\nu_3(E, F_2)$ band, the experimental absorption profile looks stronger and broader near the band origin. All these unexplained features could be also attributed to Si_2F_6O because the polyad structure of our line list completely covers this region (see Figure 2).

8. Conclusions

This work clearly demonstrated the advantage of using *ab initio* calculations for the modelling of the room-temperature absorption spectrum of the silicon tetrafluoride molecule (SiF_4). Both line positions and line intensities were computed using a new effective model including all the cold bands and most of the hot bands within the spectral range [0–2500] cm^{-1}, where the most prominent absorption features of SiF_4 are visible. To achieve this end, first full-dimensional potential energy and dipole moment surfaces were developed using high-level electronic structure calculations and including high-order electronic correlation effects [CCSDT(Q)]. For the first time, the fundamental band origins of $^{28}SiF_4$ were predicted with an accuracy better than 1 cm^{-1}, without any empirical corrections. The first derivatives of our *ab initio* DMS were found to be in excellent agreement with the empirical values derived from the Raman spectrum of crystalline SiF_4 at 77 K.

The comprehensive line lists of $^{28}SiF_4$, $^{29}SiF_4$, and $^{30}SiF_4$ constructed in this work were applied to analyze the room temperature spectrum of the natural SiF_4 measured by Pacific Northwest National Laboratory (PNNL). Our analysis demonstrates that a large number of hot transitions turns out essential for achieving good agreement with observation. In many spectral regions – particularly those where $\nu_4(F_2)$ and $\nu_3(F_2)$ are involved – we have shown that the total integrated intensity of the hot transitions may exceed that of the cold bands. To significantly reduce the number of lines in our initial line lists containing almost half a billion transitions, all the weak transitions were converted into super-lines. A number of distinct features were also identified in the PNNL absorption spectrum and attributed to Si_2F_6O.

Though conventional effective empirical models can still be used to analyze low-temperature spectra, they strongly suffer at 296 K to describe spectra due to the absence of almost all the hot band transitions. Finally, reliable *ab initio* predictions are crucial to accurately extract the line intensities corresponding to both cold and hot bands. Only a support from *ab initio* model can provide such an amount of information.

The line lists developed in this work can be used for the simulation of the absorption spectrum of SiF_4 at room temperature. Our results provide valuable spectroscopic support for future high-resolution studies, particularly those focused on line intensity analysis.

References

1. Wang, H.; Wu, P.; Wu, Z.; Shi, L.; Cheng, L. New insight into the electronic structure of SiF_4: synergistic back-donation and the eighteen-electron rule. *Phys. Chem. Chem. Phys.* **2022**, *24*, 17679–17685.
2. Hada, M.; Takahashi, M.; Sakaguchi, Y.; Fujii, T.; Minami, M. Chamber in-situ estimation during etching process by SiF_4 monitoring using laser absorption spectroscopy. *Jpn. J. Appl. Phys*. **2023**, *62*, SI1013.
3. Ernst, O.C.; Uebel, D.; Brendler, R.; Kraushaar, K.; Steudel, M.; Acker, J.; Kroke, E. Silicon-28-Tetrafluoride as an Educt of Isotope-Engineered Silicon Compounds and Bulk Materials for Quantum Systems. *Molecules* **2024**, *29*, 4222.
4. Ignatov, S.K.; Sennikov, P.G.; Chuprov, L.A.; Razuvaev, A.G. Thermodynamic and kinetic parameters of elementary steps in gas-phase hydrolysis of SiF_4. Quantum-chemical and FTIR spectroscopic studies. *Russian Chemical Bulletin* **2003**, *52*, 837–845.
5. Sennikov, P.G.; Ignatov, S.K.; Schrems, O. Identification of the products of partial hydrolysis of silicon tetrafluoride by matrix isolation IR spectroscopy. *Russ. J. Inorg. Chem*. **2010**, *55*, 413–420.
6. Liu, S.; Shi, L.; Liu, G.; Xiao,W.; Zhu, H. Research on the Production of Hydrogen Fluoride from Silicon Tetrafluoride Using 2.45 GHz Microwave Plasma. *Processes* **2025**, *13*, 4.
7. Francis, P.; Chaffin, C.; Maciejewski, A.; Oppenheimer, C. Remote determination of SiF_4 in volcanic plumes: A new tool for volcano monitoring. *Geophys. Res. Lett*. **1996**, *23*, 249–252.
8. Love, S.P.; Goff, F.; Counce, D.; Siebe, C.; Delgado, H. Passive infrared spectroscopy of the eruption plume at Popocatépetl volcano, Mexico. *Nature* **1998**, *396*, 563–567.
9. Stremme, W.; Krueger, A.; Harig, R.; Grutter, M. Volcanic SO_2 and SiF_4 visualization using 2-D thermal emission spectroscopy–Part 1: Slant-columns and their ratios. *Atmos. Meas. Tech*. **2012**, *5*, 275–288.
10. Taquet, N.; Meza Hernández, I.; Stremme, W.; Bezanilla, A.; Grutter, M.; Campion, R.; Palm, M.; Boulesteix, T. Continuous measurements of SiF_4 and SO_2 by thermal emission spectroscopy: Insight from a 6-month survey at the Popocatépetl volcano. *Journal of Volcanology and Geothermal Research* **2017**, *341*, 255–268.
11. Taquet, N.; Rivera Cárdenas, C.; Stremme, W.; Boulesteix, T.; Bezanilla, A.; Grutter, M.; García, O.; Hase, F.; Blumenstock, T. Combined direct-sun ultraviolet and infrared spectroscopies at Popocatépetl volcano (Mexico). *Front. Earth Sci*. **2023**, *11*, 1062699.
12. Mori, T.; Sato, M.; Shimoike, Y.; Notsu, K. High SiF_4/HF ratio detected in Satsuma-Iwojima volcano's plume by remote FT-IR observation. *Earth Planet Sp*. **2002**, *54*, 249–256.
13. Patterson, C.W.; Pine, A.S. Doppler-limited spectrum and analysis of the $3\nu_3$ manifold of SiF_4. *J. Mol. Spectrosc*. **1982**, *96*, 404–421.
14. McDowell, R.S.; Reisfeld, M.J.; Patterson, C.W.; Krohn, B.J.; Mariena, C.; Vasquez, M.C.; Laguna, G.A. Infrared spectrum and potential constants of silicon tetrafluoride. *J. Chem. Phys*. **1982**, *77*, 4337–4343.
15. Wang, X.-G.; Sibert, E.L.; Martin, J.M.L. Anharmonic force field and vibrational frequencies of tetrafluoromethane (CF_4) and tetrafluorosilane (SiF_4). *J. Chem. Phys*. **2000**, *112*, 1353–1366.
16. Simon, F.; Cuisset, A.; Elmaleh, C.; Hindle, F.; Mouret, G.; Rey, M.; Richard, C.; Boudon, V. Unrivaled accuracy in measuring rotational transitions of greenhouse gases: THz CRDS of CF_4. *Phys. Chem. Chem. Phys*. **2024**, *26*, 12345–12357.
17. Patterson, C.W.; McDowell, R.S.; Nereson, N.G.; Krohn, B.J.; Wells, J.S.; Petersen, F.R. Tunable laser diode study of the ν_3 band of SiF_4 near 9.7 μm. *J. Mol. Spectrosc*. **1982**, *91*, 416–423.
18. Takami, M.; Kuze, H. Infrared–microwave double resonance spectroscopy of the SiF_4 ν_3 fundamental using a tunable diode laser. *J. Chem. Phys*. **1983**, *78*, 2204–2209.
19. Jörissen, L.; Prinz, H.; Kreiner, W.A.; Wenger, Ch.; Pierre, G.; Magerl, G.; Schupita, W. The ν_3 fundamental of silicon tetrafluoride. Spectroscopy with laser sidebands. *Canadian Journal of Physics* **1989**, *67*, 532-542.
20. Jörissen, L.; Kreiner, W.A.; Chen, Y-T.; Oka, T. Observation of ground state rotational transitions in silicon tetrafluoride. *J. Mol. Spectrosc*. **1986**, *120*, 233–235.
21. Boudon, V.; Manceron, L.; Richard, C. High-resolution spectroscopy and analysis of the ν_3, ν_4 and $2\nu_4$ bands of SiF_4 in natural isotopic abundance. *J. Quant. Spectrosc. Radiat. Transfer* **2020**, *253*, 107114.
22. Boudon, V.; Richard, C.; Manceron, L. High-Resolution spectroscopy and analysis of the fundamental modes of $^{28}SiF_4$. Accurate experimental determination of the Si–F bond length. *J. Mol. Spectrosc*. **2022**, *383*, 111549.

23. Merkulova, M.; Boudon, V.; Manceron, L. Analysis of high-resolution spectra of SiF_4 combination bands. *J. Mol. Spectrosc.* **2023**, *391*, 111738.
24. Richard, C.; Ben Fathallah, O.; Hardy, P.; Kamel, R.; Merkulova, M.; Rotger, M.; Ulenikov, O.N.; Boudon, V. CaSDa24: Latest updates to the Dijon calculated spectroscopic databases. *J. Quant. Spectrosc. Radiat. Transfer* **2024**, *327*, 109127.
25. Sharpe, S.W.; Johnson, T.J.; Sams, R.L.; Chu, P.M.; Rhoderick, G.C.; Johnson, P.A. Gas-Phase Databases for Quantitative Infrared Spectroscopy. *Applied Spectroscopy* **2004**, *58*, 1452–1461.
26. Rey, M.; Chizhmakova, I.S.; Nikitin, A.V.; Tyuterev, V.G. Understanding global infrared opacity and hot bands of greenhouse molecules with low vibrational modes from first-principles calculations: the case of CF_4. *Phys. Chem. Chem. Phys.* **2018**, *20*, 21008.
27. Papoušek, D.; Aliev, M.R. *Molecular Vibrational-Rotational Spectra. Theory and Applications of High Resolution Infrared, Microwave and Raman Spectroscopy of Polyatomic Molecules*; Elsevier Scientific Pub. Co: Amsterdam, Oxford, New York, 1982.
28. Knizia, G.; Adler, T.B.; Werner, H.-J. Simplified CCSD(T)-F12 methods: Theory and benchmarks. *J. Chem. Phys*. **2009**, *130*, 054104.
29. Werner, H.-J.; Knowles, P.J.; Manby, F.R.; Black, J.A.; Doll, K.; Heßelmann, A.; Kats, D.; Köhn, A.; Korona, T.; Kreplin, D.A.; Ma, Q.; Miller, T.F.; Mitrushchenkov, A.; Peterson, K.A.; Polyak, I.; Rauhut, G.; Sibaev, M. The Molpro quantum chemistry package. *J. Chem. Phys.* **2020**, *152*, 144107.
30. Werner, H.-J.; Knowles, P.J.; *et al*. MOLPRO, version 2019.2, a package of ab initio programs. https://www.molpro.net (accessed May 16, 2025).
31. Egorov, O.; Rey, M.; Kochanov, R.V.; Nikitin, A.V.; Tyuterev, V. High-level ab initio study of disulfur monoxide: Ground state potential energy surface and band origins for six isotopic species. *Chem. Phys. Lett*. **2023**, *811*, 140216.
32. Mester, D.; Nagy, P.R.; Csóka, J.; Gyevi-Nagy, L.; Szabó, P.B.; Horváth, R.A.; Petrov, K.; Hégely, B.; Ladóczki, B.; Samu, G.; Lőrincz, B.D.; Kállay M. Overview of Developments in the MRCC Program System. *J. Phys. Chem. A* **2025**, *129*, 2086.
33. Kállay, M.; Nagy, P.R.; Mester, D.; Gyevi-Nagy, L.; Csóka, J.; Szabó, P.B.; Rolik, Z.; Samu, G.; Hégely, B.; Ladóczki, B.; Petrov, K.; Csontos, J.; Ganyecz, Á.; Ladjánszki, I.; Szegedy, L.; Farkas, M.; Mezei, P.D.; Horváth, R.A.; Lőrincz, B.D. MRCC, a quantum chemical program suite. https://www.mrcc.hu (accessed May 16, 2025).
34. Burtsev, A.P.; Bocharov, V.N.; Ignatov, S.K.; Kolomiitsova, T.D.; Sennikov, P.G.; Tokhadze, K.G.; Chuprov, L.A.; Shchepkin, D.N.; Schrems, O. Integral intensities of absorption bands of silicon tetrafluoride in the gas phase and cryogenic solutions: Experiment and calculation. *Opt. Spectrosc*. **2005**, *98*, 227–234.
35. Haas, C.; Hornig, D.F. Calculation of Dipole Derivatives from Infrared Reflection Spectra or Raman Spectra of Crystals. *J. Chem. Phys*. **1957**, *26*, 707.
36. Bernstein, E.R.; Meredith, G.R. Raman spectra of SiF_4 and GeF_4 crystals. *J. Chem. Phys*. **1977**, *67*, 4132–4138.
37. Rey, M. Novel methodology for systematically constructing global effective models from ab initio-based surfaces: A new insight into high-resolution molecular spectra analysis. *J. Chem. Phys*. **2022**, *156*, 224103.
38. Rey, M. Group-theoretical formulation of an Eckart-frame kinetic energy operator in curvilinear coordinates for polyatomic molecules. *J. Chem. Phys.* **2019**, *151*, 024101.
39. Watson, J.K.G. Simplification of the molecular vibration-rotation hamiltonian. *Molecular Physics*, **1968**, *15*, 479–490.
40. Egorov, O.; Nikitin, A.; Rey, M.; Rodina, A.; Tashkun, S.; Tyuterev, V. Global modeling of NF_3 line positions and intensities from far to mid-infrared up to 2200 cm^{-1}. *J. Quant. Spectrosc. Radiat. Transfer* **2019**, *239*, 106668.
41. Rey, M.; Chizhmakova, I.S.; Nikitin, A.V.; Tyuterev, V.G. Towards a complete elucidation of the ro-vibrational band structure in the SF_6 infrared spectrum from full quantum-mechanical calculations. *Phys. Chem. Chem. Phys.* **2021**, *23*, 12115–12126.
42. Egorov, O.; Rey, M. First Ab Initio Line Lists for Triatomic Sulfur-Containing Molecules: S_2O and S_3. *J. Phys. Chem. A* **2024**, *128*, 8144–8158.
43. Rey, M.; Viglaska, D.; Egorov, O.; Nikitin, A.V. A numerical-tensorial "hybrid" nuclear motion Hamiltonian and dipole moment operator for spectra calculation of polyatomic nonrigid molecules. *J. Chem. Phys*. **2023**, *159*, 114103.
44. Egorov, O.; Rey, M.; Viglaska, D.; Nikitin, A.V. Rovibrational Line Lists of Triplet and Singlet Methylene. *J. Phys. Chem. A* **2024**, *128*, 6960–6971.
45. Gamache, R.R.; Vispoel, B.; Rey, M.; Nikitin, A.; Tyuterev, V.; Egorov, O.; Gordon, I.E.; Boudon, V. Total internal partition sums for the HITRAN2020 database. *J. Quant. Spectrosc. Radiat. Transfer* 2021, 271, 107713.
46. Bunker, P. R.; Jensen, P. *Fundamentals of Molecular Symmetry*; IOP Publishing, Bristol, 2004 (ISBN 0-7503-0941-5).
47. Clark, R.J.H.; Rippon, D.M. The vapor-phase Raman spectra, Raman band contour analyses, Coriolis constants, and force constants of spherical-top molecules MX_4 (M = Group IV element, X = F, Cl, Br, or I). *J. Mol. Spectrosc*. **1972**, *44*, 479–503.